Ultrabright Entangled-Photon-Pair Generation from an AlGaAs-On-Insulator Microring Resonator

Trevor J. Steiner[,1] Joshua E. Castro,[2] Lin Chang,[2] Quynh Dang,[2] Weiqiang Xie,[2] Justin Norman,[2] John E. Bowers,[1,2] and Galan Moody[2,*]

[1]*Materials Department, University of California, Santa Barbara, California 93106, USA*

[2]*Electrical and Computer Engineering Department, University of California, Santa Barbara, California 93106, USA*

Entangled-photon pairs are an essential resource for quantum-information technologies. Chip-scale sources of entangled pairs have been integrated with various photonic platforms, including silicon, nitrides, indium phosphide, and lithium niobate, but each has fundamental limitations that restrict the photon-pair brightness and quality, including weak optical nonlinearity or high waveguide loss. Here, we demonstrate a novel ultralow-loss AlGaAs-on-insulator platform capable of generating time-energy entangled photons in a $Q > 1$ million microring resonator with nearly 1000-fold improvement in brightness compared to existing sources. The waveguide-integrated source exhibits an internal generation rate greater than 20×10^9 pairs s^{-1} mW^{-2}, emits near 1550 nm, produces heralded single photons with $> 99\%$ purity, and violates Bell's inequality by more than 40 standard deviations with visibility $> 97\%$. Combined with the high optical nonlinearity and optical gain of AlGaAs for active component integration, these are all essential features for a scalable quantum photonic platform.

I. INTRODUCTION

Entanglement is the cornerstone of quantum science and technologies. Compared to matter-based quantum systems, such as electronic spins [1], optomechanical resonators [2], superconducting circuits [3], and trapped atoms and ions [4], photons are unique in their ability to generate and distribute entangled quantum states across long distances in free space or fiber networks while retaining a high degree of coherence. Following the seminal experiments demonstrating the creation of photon pairs in maximally entangled Bell states over two decades ago, parametric down-conversion in bulk nonlinear crystals has been the workhorse for quantum light generation [5]. Despite the low efficiency of bulk sources, they produce nearly indistinguishable photons with high purity and entanglement fidelity at nearly gigahertz pair generation rates, making them appealing for a wide range of experiments, including foundational tests of quantum mechanics [6,7], sensing [8],

information processing [9], and satellite-based quantum communications [10,11].

Recent advances in the fabrication of quantum photonic integrated circuits (QPICs) have enabled the functionality of bench-top nonlinear sources to be scaled down to a single chip, with a dramatic improvement in the efficiency and stability [12–15]. Silicon-based photonics is a versatile platform for QPICs owing to its relative low waveguide loss and existing foundry infrastructure developed for the telecommunications industry. State-of-the-art integrated quantum photonic circuits based on SOI are capable of implementing quantum gates between two qubits [16] and chip-to-chip teleportation [17], for example, but they have to rely on off-chip detectors that introduce significant loss, slow thermal-based active components for tuning and modulation, and off-chip high-power lasers to generate single and entangled photons due to the moderate optical nonlinearity of silicon. Other nonlinear material platforms have been developed to address some of these issues, including lithium niobate [18], aluminum nitride [19], indium phosphide [20], silicon carbide [21], and heterogeneous approaches [13,22], but each has tradeoffs including higher waveguide loss and complex fabrication that hinder the scalability and reliability. Moreover, it is not readily apparent that any of these platforms are capable of all-on-chip integration of lasers, sources, active and passive components, and detectors—all which
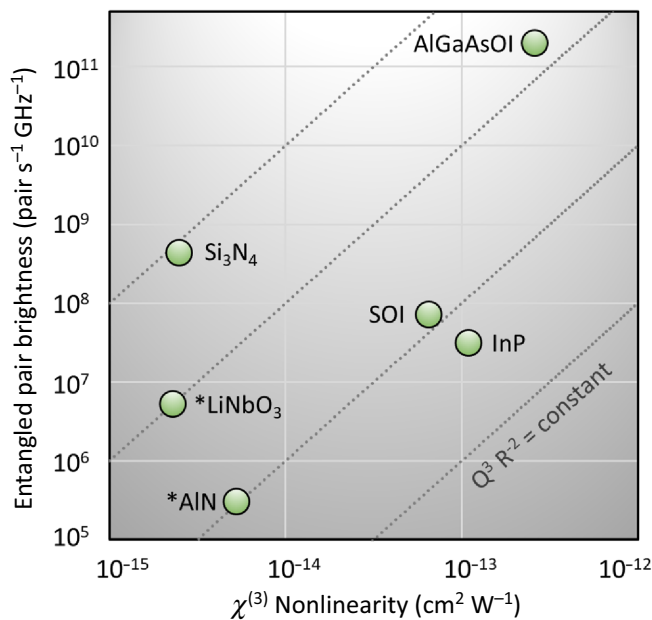

FIG. 1. The on-chip entangled-photon-pair brightness plotted as a function of the $\chi^{(3)}$ nonlinear coefficient of the material. All brightness values are normalized to 1 mW on-chip power for comparison. $LiNbO_3$ and AlN generate entangled-photon pairs via $\chi^{(2)}$ processes (as indicated by an asterisk) but they are plotted here using their $\chi^{(3)}$ coefficients for simplicity. Isolines of constant $Q^3 R^{-2}$ are illustrated by the dashed lines. The data for the materials are estimated from the references shown in Table I.

are essential for creating practical and scalable QPIC technologies [22].

Here, we report a new QPIC platform based on AlGaAs-on-insulator (AlGaAsOI) that has exciting prospects for all-on-chip quantum-information applications. Compound semiconductors have been widely used in the photonics industry due to their attractive properties of light emission and well-developed material growth and fabrication processes. They also hold great potential for nonlinear processes, since these materials usually exhibit orders-of-magnitude-higher nonlinear coefficients compared to dielectrics. However, previous compound-semiconductor photonic platforms suffer from weak optical confinement on native substrates and significant waveguide loss that has limited their utility for quantum photonic applications. Over the past few years, a novel platform, AlGaAsOI, has emerged by heterogeneously integrating (Al)GaAs onto an oxidized Si substrate that is capable of providing high-index-contrast waveguides [23]. More importantly, recent breakthroughs in the processing techniques on this platform have significantly reduced the propagation loss for AlGaAsOI waveguides. Currently, for fully etched submicron-scale AlGaAsOI waveguides, the loss is < 0.2 dB cm^{-1}, resulting in microring-resonator quality factors of $Q > 3 \times 10^6$, overperforming the SOI platform. Such high-Q resonators have enabled record-low-threshold

frequency-comb generations at 1550 nm [24,25] under a pump power at the level of tens of microwatts, which opens up an unprecedented highly nonlinear regime for integrated photonics.

In this work, we make a key step to bring the desired nonlinear properties of this platform into the quantum regime through spontaneous four-wave mixing, where pump photons tuned into resonance with a comb line near 1550 nm can be annihilated to produce time-energy entangled signal and idler pairs at adjacent comb lines [26]. We demonstrate that the combination of high Q, a small microring radius, a large $\chi^{(3)}$ nonlinearity, and a tight modal-confinement factor of AlGaAsOI results in more than a 500-fold improvement in the time-energy entangled-pair generation rate $R_{\mathrm{PG}} = 20 \times 10^9$ pairs s^{-1} mW^{-2} over the state of the art, with $97.1 \pm 0.6\%$ visibility, a > 4300 coincidence-to-accidental ratio (CAR), and heralded single-photon antibunching $g_H^{(2)}(0) < 0.004 \pm 0.01$. Figure 1 demonstrates the improvement of the AlGaAsOI-based sources over other nonlinear materials.

II. DEVICE FABRICATION

The AlGaAs photonic layer is grown by molecular-beam epitaxy (MBE). Its layer structure from top to substrate is as follows: a [001]-orientated 400-nm-thick $Al_{0.2}Ga_{0.8}As$ film on a 500-nm-thick $Al_{0.8}Ga_{0.2}As$ layer on a GaAs substrate. A 5-nm-thick Al_2O_3 film is deposited on the epilayer by atomic layer deposition (ALD) as an adhesive layer for bonding. The wafer is then bonded on to a 3-μm-thick thermal SiO_2 buffer layer on a Si substrate. The thermal SiO_2 layer is prepatterned by inductively coupled plasma (ICP) etch. The surfaces of both chips are treated by atmospheric plasma before bonding to activate the surface. After initial contact, the bonded sample is placed in an oven at $100°C$ for 12 h under 1 MPa pressure to enhance the bonding strength.

Removal of the GaAs substrate is performed in three steps. First, mechanical polishing is applied to lap the GaAs substrate down to 70 μm. Then the remaining substrate is removed by H_2O_2:NH_4OH (30:1) wet etch. Finally, the $Al_{0.8}Ga_{0.2}As$ buffer layer is selectively etched by diluted hydrofluoric (approximately 2.5%) acid, leaving only the $Al_{0.2}Ga_{0.8}As$ photonic layer on the carrier wafer.

After substrate removal, a 5-nm ALD Al_2O_3 layer is deposited on $Al_{0.2}Ga_{0.8}As$ for surface passivation, followed by a 100-nm SiO_2 layer deposition as a hard mask. The wafer is then patterned by a deep-ultraviolet (DUV) stepper using a photoresist (UV6-0.8). Prior to the photoresist coating, an antireflective (AR) coating (DUV-42P) is used to suppress the back reflection during photolithography. After exposure and development of the resist, a thermal-reflow process is applied to the wafer at $155°C$ on a hot plate for 2 min. ICP etches using O_2 and CHF_3-CF_4-O_2 gases are used to remove the AR coating and define

the hard mask, respectively, followed by another ICP etch using Cl_2/N_2 gases to pattern the $Al_{0.2}Ga_{0.8}As$ layer. After the etch, the sample is passivated by a 5-nm Al_2O_3 layer using ALD and finally clad with 1.5-μm-thick SiO_2 by plasma-enhanced chemical-vapor deposition.

III. RESULTS

A. Spontaneous four-wave mixing from AlGaAsOI microring resonators

The process of spontaneous four-wave mixing (SFWM) in a microring resonator is illustrated in Fig. 2(a). The inset depicts the fundamental concept behind SFWM, where two pump photons (denoted λ_p) are annihilated and a signal photon (λ_s) and an idler photon (λ_i) are created. This process only occurs at the resonances of the microring resonator in which quasiphase matching between the pump, signal, and idler is attained. A demonstrative microscope image of a 30-μm-radius AlGaAsOI microring resonator and pulley waveguide is shown in Fig. 2(b). The microring resonator studied in the following experiment has a radius of 13.91 μm. The width of the bus waveguide is 0.48 μm, and the ring waveguide is 0.69 μm wide. The

gap between the waveguide and the ring is 0.48 μm and the AlGaAs layer is 0.4 μm thick. The transmission spectrum of the ring resonator is shown in Fig. 2(c). The sharp troughs indicate resonance wavelengths of the microring resonator separated by the free spectral range (FSR). A high-resolution sweep of the pump comb line is shown by the blue trace in Fig. 2(d). The resonance is fitted with a Lorentzian function to determine the quality factor Q of the cavity, which is proportional to the ratio of the full width at half maximum (FWHM) of the transmission resonance to the FSR. In comparison to other microring resonators utilized for entangled-pair generation, the $Q = 1.24 \times 10^6$ measured for this device is a factor of 100 larger than for InP, approximately a factor of 10 larger than for AlN and SOI and is comparable to that of Si_3N_4, as shown in Table I.

By pumping the resonator at one of these resonance wavelengths, entangled-photon pairs are generated spontaneously at adjacent resonances through SFWM. In the experiments presented here, and shown by the dashed box in Fig. 2(c), the pump wavelength is set to be resonant with 1557.59 nm, as this resonance peak has the highest quality factor for the selected ring. As we show in the next section,
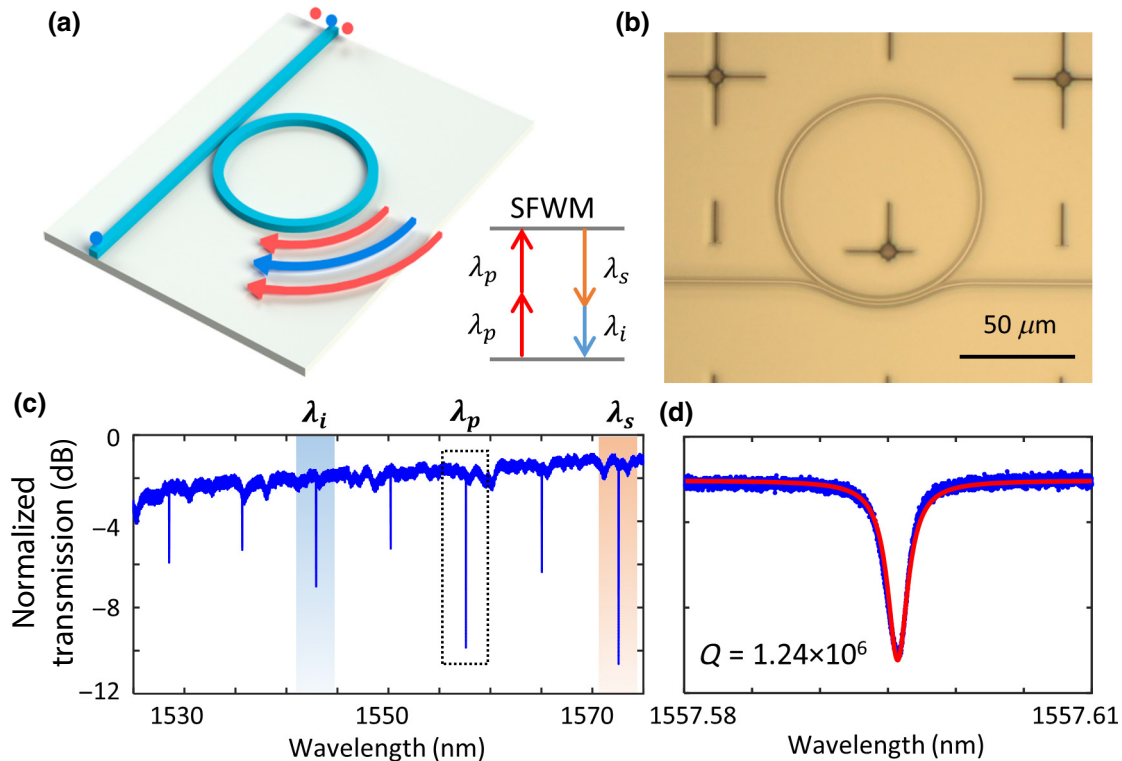

FIG. 2. (a) A schematic illustration of entangled-photon-pair generation from a photonic microring resonator. Pump photons (λ_p) are coupled into the waveguide bus and ring and are converted into signal (λ_s) and idler (λ_i) photons via spontaneous four-wave mixing (SFWM). (b) An optical-microscope image of a representative AlGaAsOI ring-resonator pulley with a 30-μm radius. (c) The resonator transmission spectrum with signal (1572-nm) and idler (1542-nm) wavelengths two free-spectral ranges away from the pump (1557-nm) resonance. (d) The resonator transmission spectrum of the pump resonance (blue trace). A $Q = 1.24 \times 10^6$ is determined from the superimposed Lorentzian fit (red trace).

TABLE I.   All values are reported for microring resonators except for LiNbO$_3$, which is acquired from a linear waveguide. The CAR, visibility, and $g_H^{(2)}$ (0) are shown for 1-MHz R_{PG}. The brightness and R_{PG} are shown normalized to a 1-mW on-chip pump power.

Platform	Type	Q	R_{PG} (GHz)	Brightness (pairs s^{-1} GHz^{-1})	CAR	Visibility	$g_H^{(2)}$	Ref.
AlGaAsOI	SFWM	1.2×10^6	20	2×10^{11}	2697 ± 260	$97.1 \pm 0.6\%$	0.004 ± 0.01	This work
AlGaAsOI	SFWM	0.91×10^6	2.65	2.65×10^{10}	–	–	–	This work
SOI	SFWM	$\sim 10^5$	0.149	7.1×10^7	532 ± 35	$98.9 \pm 0.6\%$	0.0053 ± 0.021	[29]
InP	SFWM	4×10^4	0.145	3.1×10^7	277	$78.4 \pm 2\%$	-	[20]
Si$_3$N$_4$	SFWM	2×10^6	0.004	4.3×10^8	~ 10	$90 \pm 7\%$	–	[28]
LiNbO$_3$	SPDC	–	0.023	3×10^5	668 ± 1.7	–	–	[18]
AlN	SPDC	1.1×10^5	0.006	5.3×10^6	–	–	0.088 ± 0.004	[19]

the on-chip pair generation rate depends on several factors and is given by [20,26,27]

$$R_{PG} = (\gamma 2\pi R)^2 \left(\frac{Qv_g}{\pi \omega_p R} \right)^3 \frac{v_g}{4\pi R} P_p^2, \qquad (1)$$

where R is the ring-resonator radius, γ is the nonlinear coefficient of the material, which also takes the confinement factor into account, Q is the quality factor, ω_p is the angular frequency, v_g is the group velocity at the pump wavelength, and P_p is the on-chip pump power. The quality factor Q is a critical parameter for the photon-pair generation rate as it is related to the amount of time for which resonant photons reside within the cavity and thus the amount of interaction time photons have with each other. With the pump laser set to this resonance wavelength, entangled-photon pairs are generated at adjacent multiples of the cavity FSR. In our experiments, the second-nearest-neighbor resonances highlighted in blue and orange in Fig. 2(c) are selected as the signal and idler photons, since this provides additional pump rejection through the band-pass optical filters before the single-photon detectors. Using the measured and calculated properties of our AlGaAsOI microresonators, we expect $R_{PG} = 10^{10}$ pairs s^{-1} mW^{-2}.

B. On-chip photon-pair generation rate and brightness

A schematic of the fiber-based experimental setup for entangled-pair generation is shown in Appendix A and discussed in detail in the corresponding section. Briefly, tapered fibers are used to couple the pump laser and entangled pairs onto and off the AlGaAsOI chip. After the chip, the residual pump, signal, and idler photons pass through a 3-dB splitter and the pump light is filtered using a series of tunable Fabry-Perot etalons to provide more than 130 dB of rejection in each of the signal and idler paths. The signal and idler photons are detected with superconducting-nanowire single-photon detectors (SNSPDs) with sub-40-ps timing jitter. The singles rates are shown in Fig. 3(a) for the signal and idler channels for various on-chip pump

powers. It is clear that the rates follow a P_p^2 dependence, as expected for the SFWM process. We note that these values are the raw values as detected at the SNSPDs. The idler filter path has a larger loss (19.4 dB) compared to the signal filters (13.6 dB) at their respective wavelengths, which explains the disparity between the singles rates. In addition to the filter losses, the generated signal and idler rates are also reduced due to the chip-to-fiber coupling loss and loss in the SNSPD system.

We next measure the coincidence counts by recording two-photon correlation histograms using a time-correlated single-photon counting module. From these measurements, the on-chip R_{PG} is determined by dividing the time-averaged value of the measured coincidence counts, N_c, by the total loss from the chip to the SNSPDs. These quantities are measured by separate calibration procedures. The on-chip R_{PG} for various on-chip pump powers is shown in Fig. 3(b). Unlike InP and silicon-based microresonators, we do not observe any saturation of the curve due to two-photon absorption (TPA), as expected, since the AlGaAs band-gap wavelength is shorter than 775 nm. The black dashed line fitted to the data illustrates the P_p^2 behavior as expected. From this fit, we determine a slope of 20×10^9 pairs s^{-1} mW^{-2}. To the best of our knowledge, this value is over 100 times higher than any previously reported R_{PG} to date, as shown in Table I. By normalizing the R_{PG} to the FWHM of the emission resonance (approximately 1 pm), we obtain the entangled-pair brightness $B = 2 \times 10^{11}$ pairs s^{-1} GHz^{-1} (normalized to 1 mW on-chip power), which is more than a 500-fold improvement upon previous state-of-the-art microresonators based on Si$_3$N$_4$ [28] and more than 1000 times brighter than SOI [29].

C. Coincidence-to-accidental ratio

Another important metric of entangled-photon-pair sources is the coincidence-to-accidental ratio (CAR). An example histogram utilized to determine the CAR is shown in the Appendix C (Fig. 8). The CAR versus the R_{PG} is shown in Fig. 3(c). The CAR is calculated as the FWHM
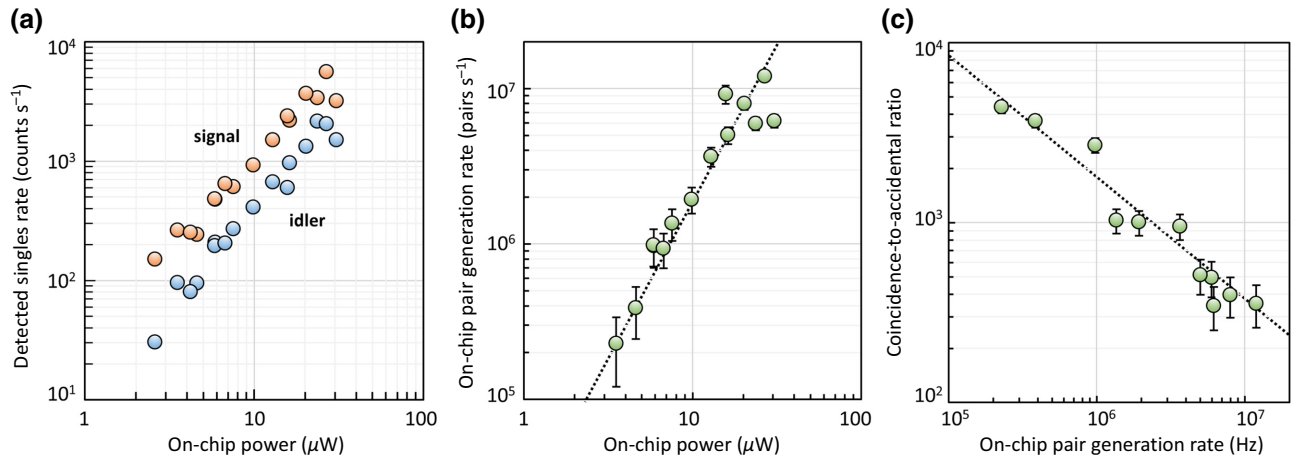
FIG. 3. (a) Corrected detected singles rates versus the on-chip pump power. The difference in the generated singles rates is due to the difference in the filter loss in the two channels (19.4 dB for the idler and 13.6 dB for the signal). (b) The on-chip pair generation rate versus the on-chip pump power. The dashed line is a fit to the data, yielding a pair generation rate of 20×10^9 pairs s^{-1} mW^{-2} (c) The coincidence-to-accidental ratio (CAR) versus the on-chip pair generation rate.

of the signal-idler coincidence histogram measured as a function of the interchannel delay divided by the background counts across a similar time window. The highest CAR we measure is 4389, when the R_{PG} is 2.3×10^5 pairs s^{-1}. At the highest R_{PG} measured here (12×10^6 pairs s^{-1}), the CAR is equal to 353. The CAR decreases with increasing pump power as P_p^{-1}, as expected and as shown by the dashed line in Fig. 3(c). We are not able to measure higher CAR at lower on-chip pump power, since the majority of the histogram time bins have zero registered background counts from our SNSPDs at these powers even for integration times up to 1.5 h. For comparison, CAR values for an on-chip $R_{PG} = 10^6$ pairs s^{-1} are shown in Table I for various photonic entangled-pair sources. Our reported value is a factor of 4 larger than the next-highest reported value at this R_{PG} (LiNbO$_3$ periodically poled waveguide).

D. Time-energy entanglement

The generated signal-idler pair is expected to exhibit time-energy entanglement [30,31], which can be measured through a Franson-type two-photon interference experiment as depicted in Fig. 4(a) [32,33]. Signal and idler photons travel through the unbalanced Mach-Zehnder interferometer and then are separated by a 3-dB splitter and band-pass filters before arriving at the SNSPDs. The interferometer path-length difference is set such that the propagation delay $\Delta t = 40$ ns is longer than the single-photon coherence time $\tau_c \approx 5.7$ ns in order to avoid single-photon interference at the detectors, but shorter than the laser coherence time τ_L. In this case, the signal and idler photons

can travel along either the short [S] or long [L] paths, allowing a total of four possible permutations.

The differences in photon arrival times between the two paths are illustrated in Fig. 4(b). We can express the two-photon state as a summation over $|ij\rangle$, where the i (j) index is the path the signal (idler) photon travels, with $i,j = $ [S,L]; however, postselection allows for the different states to be distinguished. The side peaks arise from photons traveling along the $|LS\rangle$ or $|SL\rangle$ paths and are offset from zero delay by Δt. The central peak at zero delay is due to both photons taking the same paths, $|SS\rangle$ or $|LL\rangle$. Because these states are indistinguishable, the two-photon state is expressed as $\frac{1}{\sqrt{2}}(|SS\rangle + exp(i\phi_{i+s})|LL\rangle)$. By inserting a voltage-controlled fiber phase shifter into the short path and sweeping the phase, two-photon interference is observed as shown in Fig. 4(b) for two different phases, $\varphi_{s+i} = 0.4\pi$ and π. The coincidence counts versus the phase are shown in the bottom panel of Fig. 4(c). Proof of photon entanglement requires the Clauser-Horne interference-pattern visibility $V \geq 70.7\%$ [34,35]. Calculated from the raw data (fitted data), we obtain $V = 95\%$ ($V = 97.1\%$), measured when the on-chip R_{PG} is approximately 1×10^6 pairs s^{-1}. For on-chip powers of approximately 5 μW (R_{PG} of approximately 4×10^5 pairs s^{-1}) and approximately 15 μW (R_{PG} of approximately 4×10^6 pairs s^{-1}), we measure raw visibilities of 96% and 94%, respectively. We expect that the visibility may increase further with a reduction in the pump power but the goal is to demonstrate the maximum visibility and the highest pump powers (e.g., pair generation rate) as possible. In this case, we do not examine higher pump powers above 15 μW in order to avoid reaching the lasing threshold of the microresonator, which would result in uncorrelated
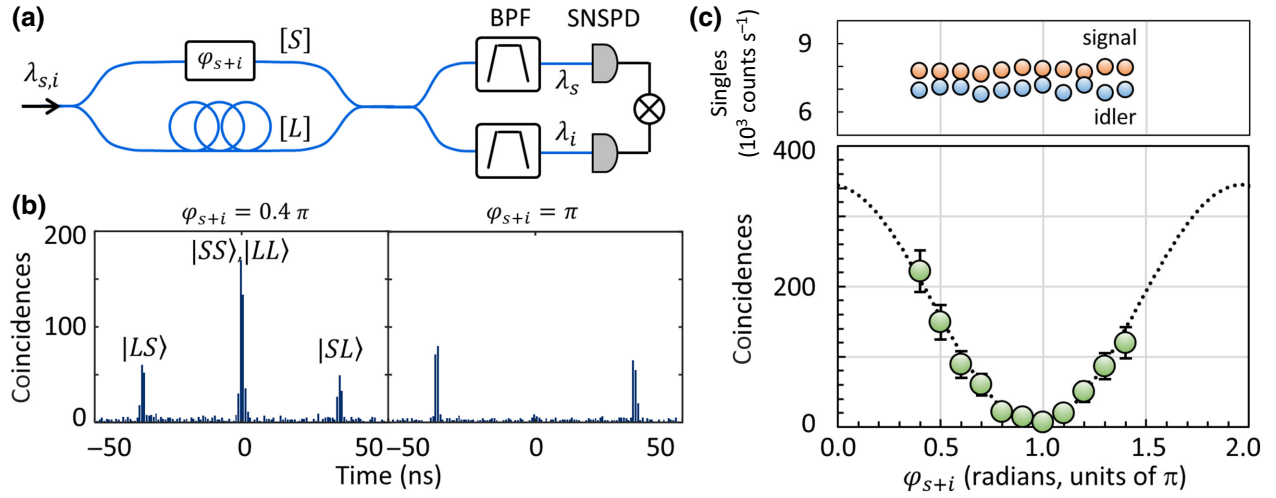
FIG. 4. (a) A schematic illustration of the setup for the two-photon interference experiment using a fiber-based folded Franson interferometer: BPF, band-pass filter; [S] ([L]), short (long) interferometer path; SNSPD, superconducting-nanowire single-photon detector. (b) Coincidence histograms for different interferometric phase $\phi_{s+i} = 0.4\pi$ and π, respectively. (c) Singles counts (top) measured with the interferometer setup simultaneously with the two-photon interference (bottom). The visibility of the raw (fitted) data yields 95% (97.1%).

background counts that would reduce the entanglement visibility. These measurements confirm the high quality of the time-energy entangled-pair source, as illustrated by the variation of the two-photon coincidences and the constant signal and idler singles rates versus the applied phase shift, indicating the absence of single-photon interference.

E. Heralded single-photon generation

Heralded $g_H^{(2)}$ measurements are performed via threefold coincidence detection with a third detector. The signal photons are sent to one SNSPD as the herald. The idler photons are sent into a 3-dB fiber beam splitter with the outputs connected to the other SNSPD and a single-photon avalanche diode (SPAD). Using the TCSPC module, we record singles counts from the heralding detector (N_A), coincidence counts between the heralding detector and each of the idler detectors (N_{AB} and N_{AC}), and the threefold coincidence counts N_{ABC}. A coincidence window of 4 ns is used as determined from the twofold coincidence histogram width. The timing between the channels is calibrated with separate coincidence measurements and the delays adjusted accordingly. Within the total integration time of 300 min, we do not observe any threefold coincidence counts above the background; thus $g_H^{(2)}(0)$ is estimated from the raw counts (i.e., without background subtraction) through the expression ($N_{ABC}N_A/N_{AB}N_{AC}$). With this calculation, we report $g_H^{(2)}(0) = 0.004 \pm 0.01$ (the measurement uncertainty is determined from the Poissonian statistics of N_A, N_{AB}, N_{AC}, and N_{ABC}, and a lower uncertainty resulting in $g_H^{(2)}(0) \geq 0$ is expected with longer measurement times).

IV. CONCLUSION

Strategies to improve on-chip entangled-photon-pair generation have typically focused on improving the quality factor of microcavities while simultaneously reducing the cavity length. The exploration of new material platforms with higher nonlinear coefficients has been limited by the attainable quality factor of these materials. By leveraging our recent advances in compound semiconductor nanofabrication [25], we achieve ultralow waveguide loss (< 0.4 dB cm^{-1}) and a high microring-resonator quality factor ($Q > 1$ million). In this work, we report the first demonstration of entangled-photon-pair generation in AlGaAsOI. The high Q and large third-order nonlinearity of AlGaAs lead to a more than 500-fold improvement of the on-chip pair brightness compared to all other photonic platforms, as shown in Fig. 1. The photon quality also remains exceptional, with a Bell-state violation measurement revealing a $97.1 \pm 0.6\%$ visibility, a coincidence-to-accidental ratio of more than 4350 limited by the loss in our optical setup, and a heralded single-photon $g_H^{(2)}(0) = 0.004 \pm 0.01$. Collectively, these values yield an ultrahigh-quality entangled- and heralded-photon source that surpasses sources from all other integrated photonic platforms, as shown in Table I. In addition to the entangled-pair source demonstrated here, AlGaAsOI has remarkable potential for all-on-chip QPIC development compared to existing platforms. First, the on-chip integration of tunable excitation laser sources can be naturally incorporated into the epitaxial growth process of the AlGaAs photonic layer [36]. AlGaAsOI is also distinguished by high index contrast for tight modal confinement [37], has negligible two-photon absorption at 1550 nm with a proper Al portion [38], exhibits a large

$\chi^{(2)}$ nonlinearity for high-speed electro-optic modulation [39] and a strong piezo-optic effect for optomechanic cavities [40], and ultraquiet superconducting-nanowire single-photon detectors (SNSPDs) have been integrated with GaAs/AlGaAs waveguides [41]. The possible application space is extraordinarily broad (Fig. 5), ranging from ground-to-satellite communications and quantum teleportation to all-on-chip quantum-information processing and boson sampling [10,11,17,42].

Such high performance dramatically impacts the selection of quantum sources in QPICs. In recent years, self-assembled quantum dots (QDs) embedded in optical microcavities have become state of the art in generating quantum light, since they are capable of producing entangled-photon pairs and single photons at rates thought impossible for probabilistic nonlinear sources [12]. However, those photon sources have to be operated at cryogenic temperature and their selective growth is also quite challenging, which hinders their system-level scaling. In addition, the emitted photon energy of an InAs QD usually lies outside of the telecommunications wavelength (C band), adding considerable inconvenience with regard to information processing and transmission. Some other on-demand quantum photon sources, such as GaN QDs and carbon nanotubes, can be operated at room temperature and some of them also operate in the C band; however,

so far, their photon generation rates are limited. Therefore, the more than 2- (4-) orders-of-magnitude improvement in the pair generation rate (brightness) enabled by AlGaAsOI makes probabilistic sources significantly more competitive by combining the advantages of room-temperature operation, the higher quality of the produced single photons and entangled-photon pairs, and the intrinsic scalability afforded by microring-resonator structures.

Although the AlGaAsOI platform boasts groundbreaking values in photon-pair generation, much exciting work remains to be done. Brighter entanglement sources require lower on-chip pump power for a given pair generation rate. This relaxes the requirements of on-chip filters for pump rejection. Compared to current state-of-the-art QPICs based on SOI, the lower waveguide loss of AlGaAsOI can significantly reduce the overall system loss, allowing more components to be accommodated for applications requiring system-level integration, such as multiqubit quantum computation. Another advantage is on the tuning side: AlGaAs has a factor-of-2 larger thermo-optic coefficient than that of Si, which can enable more efficient thermotuners. The electro-optic and piezo-optic effects provide a novel tuning scheme for scenarios where high-speed operation or cryogenic temperatures are required. Therefore, AlGaAsOI holds exciting prospects for all-on-chip quantum photonic integrated
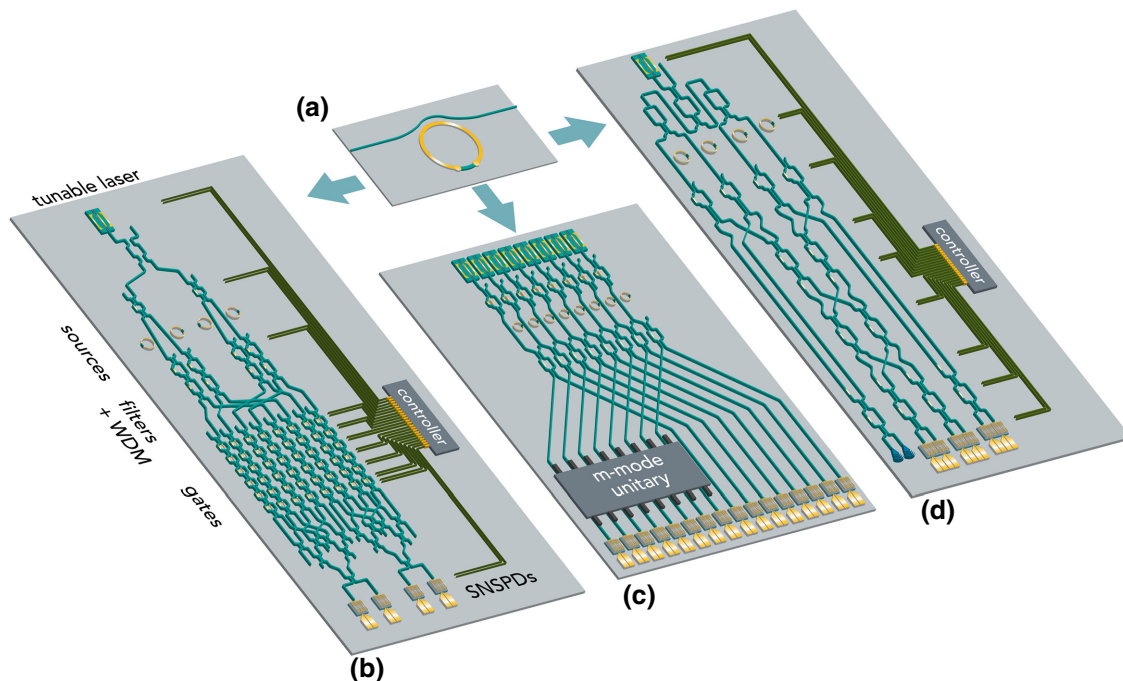

FIG. 5. (a) The tunable AlGaAs-on-insulator (AlGaAsOI) microring-resonator entangled-photon-pair source. The AlGaAsOI platform enables the large-scale integration of active and passive quantum photonic components, including tunable lasers, nonlinear quantum light sources, filters and wavelength-division multiplexing (WDM), superconducting-nanowire single-photon detectors (SNSPDs), and microcontrollers. These components can be monolithically integrated for all-on-chip quantum photonic circuits, including (b) quantum gates for optical computing, (c) m-mode unitary operations for boson sampling, and (d) Bell-state measurements for chip-to-chip teleportation of quantum states.

circuits, where tunable lasers, nonlinear sources, distributed-Bragg-grating reflectors, Mach-Zehnder interferometers, high-speed electro-optic modulators, demultiplexers, and chip-to-fiber couplers can be monolithically integrated into the same AlGaAsOI platform without the need for complex heterogeneous integration techniques. Moreover, the large $\chi^{(2)}$ nonlinearity of AlGaAs [43] can be leveraged for tuning various photonic elements at the cryogenic temperatures needed for superconducting-nanowire single-photon detector integration and operation.

All-on-chip integration with this platform will significantly improve the performance of our devices by reducing the optical loss without sacrificing functionality, as has been demonstrated on SOI [44–47]. The combination of our sources with low-loss high-performing photonic components and detectors could lead to an orders-of-magnitude improvement in the computation and communication rates of quantum processors, quantum transceivers, and the entanglement distribution needed for quantum networks.

ACKNOWLEDGMENTS

APPENDIX A: EXPERIMENTAL DESIGN

The full experimental design is depicted in Fig. 6. For the measurement of the singles and coincidence counts, the interferometer shown in Fig. 6 (the short and long arm with the piezo-electric phase shifter) is bypassed. Other than this change for the singles and coincidence measurements, the rest of the experimental design remains consistent. A continuous-wave Koshin Kogaku LS601A series precision tunable laser source is stepped from approximately 0.1 nm below the resonance wavelength of the microring resonator to the resonance wavelength. The laser sweep starts below the actual resonance wavelength because the ring resonance red shifts due to local heating of the resonator as the wavelength approaches the resonance. The laser is set to its maximum output power of 2.0 dBm (15.8 mW) and sent through a variable optical attenuator (VOA) to allow
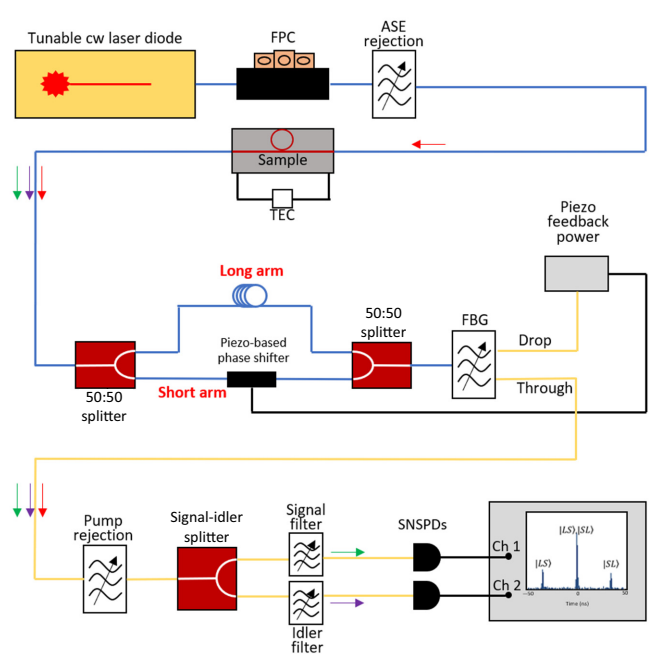

FIG. 6. A schematic of the experimental setup for a fiber-based folded Franson-type interferometer. The tunable cw laser diode is swept and held at the resonance wavelength of the microring resonator. The laser is sent through amplified-spontaneous-emission (ASE) rejection filters and coupled via lensed fiber onto and off of the photonic chip. The light is split into a short and a long arm of an interferometer. A piezo-based phase shifter is used to modify the phase of the photons that travel through the long arm. The pump photons are removed via an FBG and filters on the signal and idler channels. The signal and idler channels are coupled to SNSPDs to determine the count rates.

for adjustment of the input power into the chip. Etalon-based tunable fiber-optic filters are placed after the VOA to provide sideband filtering of the laser. After the filters, a 99:1 fiber-based splitter is used to monitor the input power onto the chip. A lensed fiber with a numerical aperture of 0.11 is used to couple the light onto and off of the photonic chip. The coupling loss is approximately 5 dB per facet and is documented for each experiment. The lensed fiber is oriented such that the incoming light is in transverse-electric mode. The temperature of the chip is maintained using a thermoelectric cooler that is set to 20°C. A fiber Bragg grating (FBG) is used after the chip for pump rejection, with the drop channel used to monitor the power output from the chip during the experiment. The remaining light from the FBG is split using a 3-dB fiber-based beam splitter and sent to the signal and idler filter channels. An array of four etalon-based tunable fiber-optic filters is used for a total pump suppression of over 150 dB. The singles counts are monitored using SNSPDs from PhotonSpot, operating at 0.77 K. Using a time-correlated single-photon counting (TCSPC) module, the signal and idler counts are recorded for 10 min and averaged. The scan is started with the laser

set to a slightly off-resonance wavelength to determine the background counts on the detectors (from both the dark counts of the system and any pump photons that reach the detector). An example scan is included in Appendix B.

After collecting the raw count data from the TCSPC module, the count rates are corrected to account for the filter losses present in each channel as well as the background counts present before the laser reaches the resonance wavelength. The background counts are taken as the 1 min average of the counts on each detector before the laser sweep begins. To assess the loss at each filter, the laser is set to the wavelength of the signal (idler) and each of the filters on the signal (idler) channel is assessed for the loss at that wavelength. The total loss from all of the filtering and the 3-dB beam splitters is 19.4 dB for the idler channel and 13.6 dB for the signal channel (in addition to the approximately 5 dB facet loss). This variation is due to the different losses in the etalon-based filters. The singles counts of both the signal and the idler are fitted on a quadratic scale as shown in the main text.

To complete the coincidence measurements, the TCSPC module is set to trigger when a photon arrives on the signal channel and to measure the difference in arrival time on the idler channel. The data are collected with integration times between 10 and 180 min, depending on the on-chip power. Larger integration times are required for lower optical powers, as the coincidence-to-accidental calculation requires nonzero accidental counts. Contributors to the accidental counts include lost pairs, dark counts, and excess pump photons. Since almost zero pump photons reach the detectors at low input powers, the accidental counts are very low and require long integration times.
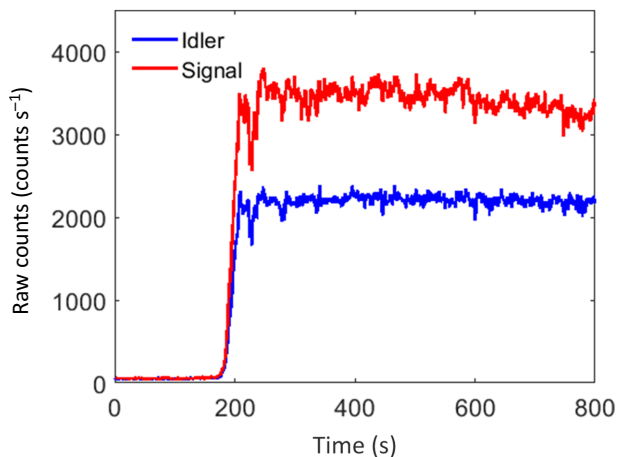
APPENDIX B: EXAMPLE SINGLES SCAN

To determine the singles counts for the signal and idler channels, the pump laser is swept from an off-resonance wavelength to the resonance wavelength and held on resonance for 10 min. An example scan for an on-chip power of -15.14 dBm (30.6 μW) is shown in Fig. 7. The initial counts represent the off-resonance counts on the detector. Ideally, these counts would be identical to the dark counts of the SNSPDs, but for larger on-chip powers, some of the pump photons still reach the detectors. Starting after approximately 200 s, the laser reaches the resonance wavelength and is held at this wavelength for 10 min. The reported singles counts are the average of this 10-min window corrected for the background counts present when the laser is off resonance. The idler channel has lower counts due to a larger filter loss on this channel relative to the signal channel.

APPENDIX C: EXAMPLE COINCIDENCE MEASUREMENT

An example histogram of a coincidence measurement at -15.71 dBm (26.9 μW) is shown in Fig. 8. The coincidence counts are integrated for 10 min or until the accidental counts average to a nonzero value (longer integration times for lower powers up to 180 min). The two-photon coincidence time window is 2.4 ns, approximately the FWHM of the coincidence peak.

APPENDIX D: DATA REPRODUCIBILITY

A total of 39 microring resonators are screened to determine the structures with the highest quality factor and a

FIG. 7. An example singles scan for an on-chip power of -15.14 dBm (30.6 μW). The scan begins with the laser set to an off-resonance wavelength. The laser is then swept to the resonance wavelength, reaching the resonance wavelength at approximately 200 s. The laser is held at this wavelength for 10 min to allow for the average singles rate to be determined.
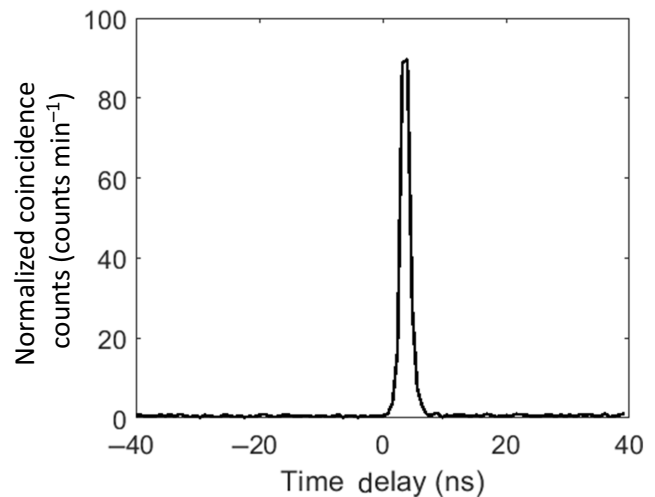

FIG. 8. An example histogram showing the normalized coincidence counts (in counts per minute) as a function of the time delay. The slight offset from 0 is due to unequal filter path lengths between the signal and idler channels.
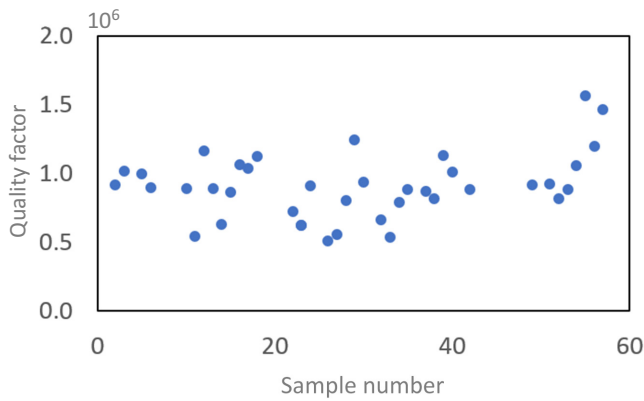
FIG. 9. The maximum quality factor for each microring-resonator sample.

small radius. The maximum quality factor of these samples is plotted versus the sample number in Fig. 9. Ring 29 is selected for an in-depth study as it has a small radius (13.91 μm) and a large quality factor (1.24 million) for its resonance near 1557 nm. The last four rings tested and shown on the plot have larger quality factors but are also much larger. Following Eq. (1), the factor of Q^3/R^2 is what dictates the pair generation rate for these resonator structures. Ring 29 is selected for detailed study as it has the highest value of this ratio. The pair generation rate for another resonator, ring 24, is included in Table I. This ring has a lower quality factor of 0.91 million and the same radius as ring 29. The measured pair generation rate of ring 24 follows the expected behavior, accounting for the lower quality factor of this resonator.

[1] E. Togan, Y. Chu, A. S. Trifonov, L. Jiang, J. Maze, L. Childress, M. V. Dutt, A. S. Sørensen, P. R. Hemmer, A. S. Zibrov, and M. D. Lukin, Quantum entanglement between an optical photon and a solid-state spin qubit, Nature **466,** 730 (2010).

[2] R. Riedinger, A. Wallucks, I. Marinković, C. Löschnauer, M. Aspelmeyer, S. Hong, and S. Gröblacher, Remote quantum entanglement between two micromechanical oscillators, Nature **556,** 473 (2018).

[3] A. A. Houck, H. E. Türeci, and J. Koch, On-chip quantum simulation with superconducting circuits, Nat. Phys. **8,** 292 (2012).

[4] D. L. Moehring, P. Maunz, S. Olmschenk, K. C. Younge, D. N. Matsukevich, L. M. Duan, and C. Monroe, Entanglement of single-atom quantum bits at a distance, Nature **449,** 68 (2007).

[5] P. G. Kwiat, K. Mattle, H. Weinfurter, A. Zeilinger, A. V. Sergienko, and Y. Shih, New High-Intensity Source of Polarization-Entangled Photon Pairs, Phys. Rev. Lett. **75,** 4337 (1995).

[6] L. K. Shalm *et al.*, Strong Loophole-Free Test of Local Realism, Phys. Rev. Lett. **115,** 250402 (2015).

[7] M. Giustina *et al.*, Significant-Loophole-Free Test of Bell's Theorem with Entangled Photons, Phys. Rev. Lett. **115,** 250401 (2015).

[8] S. Pirandola, B. R. Bardhan, T. Gehring, C. Weedbrook, and S. Lloyd, Advances in photonic quantum sensing, arXiv:1811.01969 (2018).

[9] F. Flamini, N. Spagnolo, and F. Sciarrino, Photonic quantum information processing: A review, arXiv:1803.02790 (2019).

[10] J. Yin *et al.*, Satellite-based entanglement distribution over 1200 kilometers, Science **356,** 1140 (2017).

[11] S. K. Liao *et al.*, Satellite-to-ground quantum key distribution, Nature **549,** 43 (2017).

[12] H. Wang, H. Hu, T. H. Chung, J. Qin, X. Yang, J. P. Li, R. Z. Liu, H. S. Zhong, Y. M. He, X. Ding, Y. H. Deng, Q. Dai, Y. H. Huo, S. Höfling, C. Y. Lu, and J. W. Pan, On-Demand Semiconductor Source of Entangled Photons Which Simultaneously Has High Fidelity, Efficiency, and Indistinguishability, Phys. Rev. Lett. **122,** 113602 (2019).

[13] A. W. Elshaari, W. Pernice, K. Srinivasan, O. Benson, and V. Zwiller, Hybrid integrated quantum photonic circuits (2020).

[14] J. Wang, F. Sciarrino, A. Laing, and M. G. Thompson, Integrated photonic quantum technologies (2020).

[15] G. Moody, L. Chang, T. J. Steiner, and J. E. Bowers, Chip-scale nonlinear photonics for quantum light generation, AVS Quantum Sci. **2,** 041702 (2020).

[16] X. Qiang, X. Zhou, J. Wang, C. M. Wilkes, T. Loke, S. O'Gara, L. Kling, G. D. Marshall, R. Santagati, T. C. Ralph, J. B. Wang, J. L. O'Brien, M. G. Thompson, and J. C. F. Matthews, Large-scale silicon quantum photonics implementing arbitrary two-qubit processing, Nat. Photonics **12,** 534 (2018).

[17] D. Llewellyn, Y. Ding, I. I. Faruque, S. Paesani, D. Bacco, R. Santagati, Y.-J. Qian, Y. Li, Y.-F. Xiao, M. Huber, M. Malik, G. F. Sinclair, X. Zhou, K. Rottwitt, J. L. O'Brien, J. G. Rarity, Q. Gong, L. K. Oxenlowe, J. Wang, and M. G. Thompson, Chip-to-chip quantum teleportation and multiphoton entanglement in silicon, Nat. Phys. **16,** 148 (2019).

[18] J. Zhao, C. Ma, M. Rüsing, and S. Mookherjea, High Quality Entangled Photon Pair Generation in Periodically Poled Thin-Film Lithium Niobate Waveguides, Phys. Rev. Lett. **124,** 163603 (2020).

[19] X. Guo, C. L. Zou, C. Schuck, H. Jung, R. Cheng, and H. X. Tang, Parametric down-conversion photon-pair source on a nanophotonic chip, Light: Sci. Appl. **6,** e16249 (2017).

[20] R. R. Kumar, M. Raevskaia, V. Pogoretskii, Y. Jiao, and H. K. Tsang, Entangled photon pair generation from an InP membrane micro-ring resonator, Appl. Phys. Lett. **114,** 021104 (2019).

[21] M. Guidry, K. Yang, D. Lukin, A. Markosyan, J. Yang, M. Fejer, and J. Vuckovic, Optical parametric oscillation in silicon carbide nanophotonics, Optica, 10.1364/optica.394138 (2020), arXiv:2004.13958.

[22] J.-H. Kim, S. Aghaeimeibodi, J. Carolan, D. Englund, and E. Waks, Hybrid integration methods for on-chip quantum photonics, Optica **7,** 291 (2020).

[23] M. Pu, L. Ottaviano, E. Semenova, and K. Yvind, Efficient frequency comb generation in AlGaAs-on-insulator, Optica **3,** 823 (2016).

[24] L. Chang, W. Xie, H. Shu, Q. Yang, B. Shen, A. Boes, J. D. Peters, W. Jin, C. Xiang, S. Liu, G. Moille, S.-P. Yu, X. Wang, K. Srinivasan, S. B. Papp, K. Vahala, and J. Bowers, Ultra-efficient frequency comb generation in AlGaAs-on-insulator microresonators, Nat. Commun. **11**, 1 (2020).

[25] W. Xie, L. Chang, H. Shu, J. C. Norman, J. D. Peters, X. Wang, and J. E. Bowers, Ultrahigh-Q AlGaAs-on-insulator microresonators for integrated nonlinear photonics, arXiv:2004.14537 (2020).

[26] L. G. Helt, Z. Yang, M. Liscidini, and J. E. Sipe, Spontaneous four-wave mixing in microring resonators, Opt. Lett. **35**, 3006 (2010).

[27] S. Azzini, D. Grassani, M. J. Strain, M. Sorel, L. G. Helt, J. E. Sipe, M. Liscidini, M. Galli, and D. Bajoni, Ultra-low power generation of twin photons in a compact silicon ring resonator, Opt. Express **20**, 23100 (2012).

[28] S. Ramelow, A. Farsi, S. Clemmen, D. Orquiza, K. Luke, M. Lipson, and A. L. Gaeta, Silicon-Nitride Platform for Narrowband Entangled Photon Generation, arXiv:1508.04358 (2015).

[29] C. Ma, X. Wang, V. Anant, A. D. Beyer, M. D. Shaw, and S. Mookherjea, Silicon photonic entangled photon-pair and heralded single photon generation with CAR > 12,000 and $g^{(2)(0)} < 0006$, Opt. Express **25**, 32995 (2017).

[30] J. Brendel, N. Gisin, W. Tittel, and H. Zbinden, Pulsed Energy-Time Entangled Twin-Photon Source for Quantum Communication, Phys. Rev. Lett. **82**, 2594 (1999).

[31] R. Wakabayashi, M. Fujiwara, K.-i. Yoshino, Y. Nambu, M. Sasaki, and T. Aoki, Time-bin entangled photon pair generation from Si micro-ring resonator, Opt. Express **23**, 1103 (2015).

[32] J. D. Franson, Bell Inequality for Position and Time, Phys. Rev. Lett. **62**, 2205 (1989).

[33] J. D. Franson, Two-photon interferometry over large distances, Phys. Rev. A **44**, 4552 (1991).

[34] J. F. Clauser and M. A. Horne, Experimental consequences of objective local theories, Phys. Rev. D **10**, 526 (1974).

[35] J. G. Rarity and P. R. Tapster, Experimental Violation of Bell's Inequality Based on Phase and Momentum, Phys. Rev. Lett. **64**, 2495 (1990).

[36] A. Y. Liu and J. Bowers, Photonic integration with epitaxial III–V on silicon, IEEE J. Sel. Top. Quantum Electron. **24**, 1 (2018).

[37] L. Ottaviano, M. Pu, E. Semenova, and K. Yvind, Low-loss high-confinement waveguides and microring resonators in AlGaAs-on-insulator, Opt. Lett. **41**, 3996 (2016).

[38] S. Adachi, GaAs *and Related Materials* (WORLD SCIENTIFIC, Singapore, 1994).

[39] R. Walker, N. Cameron, Y. Zhou, C. Main, G. Hoy, and S. Clements, in *International Conference on Space Optics—ICSO 2018*, edited by N. Karafolas, Z. Sodnik, and B. Cugny (SPIE, Chania, Greece, 2019).

[40] M. Forsch, R. Stockill, A. Walluck, I. Marinković, C. Gärtner, R. A. Norte, F. v. Otten, A. Fiore, K. Srinivasan, and S. Gröblacher, Microwave-to-optics conversion using a mechanical oscillator in its quantum ground state, Nat. Phys. **16**, 69 (2020).

[41] C. McDonald, G. Moody, S. W. Nam, R. P. Mirin, J. M. Shainline, A. McCaughan, S. Buckley, and K. L. Silverman, III–V photonic integrated circuit with waveguide-coupled light-emitting diodes and WSi superconducting single-photon detectors, Appl. Phys. Lett. **115**, 081105 (2019).

[42] J. B. Spring, B. J. Metcalf, P. C. Humphreys, W. S. Kolthammer, X.-M. Jin, M. Barbieri, A. Datta, N. Thomas-Peter, N. K. Langford, D. Kundys, J. C. Gates, B. J. Smith, P. G. R. Smith, and I. A. Walmsley, Boson sampling on a photonic chip, Science **339**, 798 (2012).

[43] L. Chang, A. Boes, X. Guo, D. T. Spencer, M. J. Kennedy, J. D. Peters, N. Volet, J. Chiles, A. Kowligy, N. Nader, D. D. Hickstein, E. J. Stanton, S. A. Diddams, S. B. Papp, and J. E. Bowers, Nonlinear optics: Heterogeneously integrated GaAs waveguides on insulator for efficient frequency conversion, Laser Photonics Rev. **12**, 1870044 (2018).

[44] N. C. Harris, D. Grassani, A. Simbula, M. Pant, M. Galli, T. Baehr-Jones, M. Hochberg, D. Englund, D. Bajoni, and C. Galland, Integrated Source of Spectrally Filtered Correlated Photons for Large-Scale Quantum Photonic Systems, Phys. Rev. X **4**, 041047 (2014).

[45] M. Piekarek, D. Bonneau, S. Miki, T. Yamashita, M. Fujiwara, M. Sasaki, H. Terai, M. G. Tanner, C. M. Natarajan, R. H. Hadfield, J. L. O'Brien, and M. G. Thompson, High-extinction ratio integrated photonic filters for silicon quantum photonics, Opt. Lett. **42**, 815 (2017).

[46] R. R. Kumar, X. Wu, and H. K. Tsang, Compact high-extinction tunable crow filters for integrated quantum photonic circuits, Opt. Lett. **45**, 1289 (2020).

[47] D. Grassani, S. Azzini, M. Liscidini, M. Galli, M. J. Strain, M. Sorel, J. E. Sipe, and D. Bajoni, Micrometer-scale integrated silicon source of time-energy entangled photons, Optica **2**, 88 (2015).